Austenite to bainite phase transformation in the heat-affected zone of a high strength low alloy steel

A. Lambert-Perlade [a], A.F. Gourgues [b,*], A. Pineau [b]

[a] *IRSID, Arcelor Research and Development, Voie Romaine, 57283 Maizières-lès-Metz cedex, France*
[b] *Ecole des Mines de Paris, Centre des Matériaux, UMR CNRS 7633, B.P. 87, 91003 Evry cedex, France*

Abstract

The austenite to bainite phase transformation was investigated in a low alloy structural steel after simulated welding heat treatment, by means of light microscopy, electron backscatter diffraction and transmission electron microscopy. Upper bainite packets result from the growth of groups of laths having close crystallographic orientations but highly misoriented habit planes. Self-accommodation of the transformation eigenstrain was evaluated for various bainite configurations using a micromechanical model. The observed pairs of variants seem to help limiting plastic strain in the austenite phase, thus enhancing growth of the bainite phase during cooling.
© 2004 Acta Materialia Inc. Published by Elsevier Ltd. All rights reserved.

Keywords: Bainitic steels; Welding; Phase transformation; Electron backscattering diffraction; Mean field analysis

1. Introduction

High strength low alloy steels have been developed for many years and achieve now high tensile properties and good toughness, especially through refinement of the microstructure and by applying efficient welding conditions characterised by high heat inputs. However, significant austenite grain growth may occur in the heat-affected zone of welded joints, leading to bainitic microstructures after completion of the weld. These microstructures are known to be sometimes sensitive to cleavage cracking, especially when some austenite is retained after the bainite transformation, leading to martensite–austenite (M–A) constituents [1–3]. These M–A constituents may be located between bainitic laths as well as at prior austenite grain boundaries. They are intimately related to the incomplete austenite to bainite phase transformation phenomenon.

To combine at best economic welding and safety against brittle failure, it is essential to understand the mechanism of phase transformations in the heat-affected zone and the key effects of the microstructure on the resistance to brittle fracture. The cleavage fracture resistance of bainitic microstructures is closely related to both prior austenite grains and bainite packets [4–6]. The definition of bainite packets is still controversial and optical microscopy may easily give a wrong impression so that sophisticated methods have to be used. Recent results obtained using the electron backscatter diffraction (EBSD) technique help to distinguish between "morphological" packets (as appearing in micrographs) and "crystallographic" packets, (bainite areas delimited by high-angle boundaries) [7]. The relevant microstructural unit controlling cleavage crack propagation is the crystallographic packet [7–9], since only high-angle (misorientation $> 40°$) bainite packet boundaries can efficiently stop the propagation of brittle cleavage microcracks. The crystallographic packet size strongly depends on the characteristics of the austenite to bainite phase transformation. Up to now, the mechanism of bainite formation in low carbon steels under welding conditions has only scarcely been studied in detail at the

*Corresponding author. Tel.: +33-1-60-76-30-66; fax: +33-1-60-76-31-50.

E-mail address: anne-francoise.gourgues@ensmp.fr (A.F. Gourgues).

scale of the former austenite grain (typically 50–100 μm for the coarse-grained heat-affected zone).

The aim of the present study is to investigate the crystallographic packets, which are key factors controlling brittle cleavage fracture. The study focuses on the morphological and crystallographic aspects of the austenite to bainite phase transformation in a high strength low alloy steel used for structural components, e.g., for offshore applications. For the sake of simplicity, two microstructures representative of the coarse-grained heat-affected zone were studied by the thermal simulation technique.

2. Materials and experimental procedures

2.1. Materials

The steel chosen for the study was provided as a 40-mm thick plate obtained after thermomechanical controlled processing. Its chemical composition was 0.07C–0.32Si–1.5Mn–0.16Cu–0.12Mo–0.014Nb–0.002V (wt%). All specimens were cut from mid-thickness material along the transverse direction. The microstructure in this area was ferrite–pearlite with a mean ferrite grain size of 10 μm. Its room temperature tensile properties at mid-thickness are: 0.2% proof stress = 433 MPa; ultimate tensile strength = 534 MPa; fracture elongation = 22%. The mechanical and fracture properties of this steel have been characterised and reported elsewhere [9].

Simulated welding thermal cycles were applied to 5 mm diameter blanks by means of a Gleeble 1500 thermal-mechanical simulator. Two thermal cycles were chosen, corresponding to medium (MI) and high (HI) heat input welding, respectively. For this steel, the MI cycle corresponds to the upper end of the heat input range in usual industrial conditions. For both cycles, the area of interest in the specimen was heated at 520 °C s^{-1} up to T_{p_1} = 1250 °C, and then immediately cooled with a cooling time between 800 and 500 °C, $\Delta t^{8/5}$, of 25 and 120 s for MI and HI cycles, respectively. The corresponding phase transformation temperatures (as measured by dilatometry) are given in Table 1. The standard deviation is about ±7 °C. Due to the slower cooling rate, the HI microstructure is expected to be coarser than the MI microstructure. The resulting microstructures will be referred to as "fully transformed" MI and HI

microstructures, respectively, despite the presence of a few percents of residual austenite after cooling down to room temperature. To investigate the mechanisms of bainite packet formation, some MI and HI cycles were interrupted by a martensitic quench at various stages of the welding cycle, namely, after transformation of 5%, 10%, 30% and 40% of austenite into bainite. Corresponding microstructures will be referred to as "partially transformed", although the residual austenite phase was transformed into martensite after quenching.

2.2. Metallographic techniques

The heat-treated samples were cut near the monitoring thermocouple and then polished using conventional metallographic techniques and observed by light microscopy and scanning electron microscopy (SEM). Some of them were also electrolytically polished and analysed using EBSD in the SEM. This technique allows the determination of local crystallographic orientations and has already been successfully used with bainite, acicular ferrite and lath martensite microstructures [7,8,10–12].

Thin foils of the fully transformed microstructures were also examined by transmission electron microscopy (TEM) after careful twin-jet electropolishing. Misorientations between laths were determined by Kikuchi pattern indexation.

3. Experimental results

In this section, the fine scale structure of bainite packets is first shown to consist of groups of parallel laths. Then, the spatial and crystallographic arrangements of these groups are addressed at the scale of the former austenite grain.
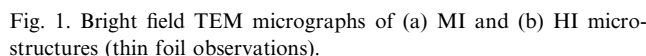
3.1. TEM investigation of bainite packets

From TEM observations, both MI and HI microstructures exhibit well-defined, highly dislocated laths (Fig. 1). Fine cementite and retained austenite particles were observed between the laths, and no intralath carbide was observed. Thus, these microstructures are considered as "upper bainite" according to both lath morphology and carbide distribution [13,14]. Due to the

Table 1
Transformation temperatures (°C) measured using dilatometry during simulated welding thermal cycles

Cycle	Heating		Cooling						
	Ac_1	Ac_3	Ar_3	5%	10%	30%	45%	90%	Ar_1
MI	758	950	618	582	570	551	540	500	449
HI	750	945	665	638	628	612	604	565	510

On cooling, fractions are normalised by the fraction of austenite actually transformed after cycle completion (>0.95).

Fig. 1. Bright field TEM micrographs of (a) MI and (b) HI microstructures (thin foil observations).

Fig. 2. Selected area diffraction pattern taken at the interface between retained austenite and bainite in the HI microstructure. The zone axis is $(011)^*_\gamma//(111)^*_\alpha$ in the reciprocal space.

Table 2
Metallurgical properties of the MI and HI microstructures

Cycle	MI	HI
Mean γ grain size (light microscopy) (μm)	56	76
Mean (%) M–A + carbides (light microscopy)	4.5	6.0
% Retained austenite (X-ray diffraction)	2.3 ± 0.5	4.0 ± 0.4
Mean crystallographic bainite packet size (EBSD) (μm)	12	15
Mean lath thickness (TEM) (μm)	0.9	1.3
Mean misorientation angle between neighbour laths (TEM)	$3.6 \pm 0.5°$	$3.9 \pm 0.5°$

lower cooling rate, bainite laths are thicker and lath boundaries are wavier for the HI microstructure than for the MI microstructure.

The austenite to bainitic ferrite orientation relationships were investigated using selected area diffraction patterns of bainite and of "blocky" retained austenite particles, which were easily found in the HI microstructure. The orientation relationships are close to the Kurdjumov–Sachs (KS) [15] (as in Fig. 2) or Nishiyama–Wassermann (NW) [16,17] orientation relationships, and always well within the Bain zone, i.e., within 10° from the $45°\langle100\rangle_\gamma$ Bain orientation relationship.

The misorientation angle (in fact, the minimum misorientation angle) between parallel neighbouring bainitic laths was always low, i.e., between 0.5° and 9°, with a mean value of 3.5–4° (Table 2). Unlike in martensite [12], lower bainite [8], or even upper bainite in steels having higher carbon contents [18], parallel neighbouring laths were here always separated by low-angle boundaries. These groups of parallel laths will be denoted hereafter as "bainite groups". A few "covariant packets", consisting of morphologically parallel, but highly crystallographically misoriented bainite laths (as
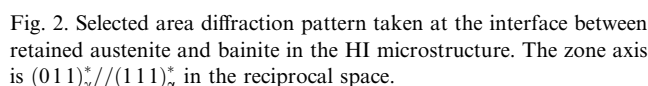
reviewed by Kalwa et al. [19]) were also found. Thus, in both microstructures, bainite packets consist of "bainite groups" having close crystallographic orientations. These groups are the basic units of the bainite packets considered hereafter.

3.2. Bainite packet morphology

After interrupted heat treatments, a mixed bainite–martensite microstructure was obtained, with the martensite phase arising from the transformation of austenite upon quenching. The bainite and martensite phases could easily be distinguished from each other using light microscopy after 1% sodium disulphite etching (Fig. 3). The bainite transformation is very heterogeneous, at least from two-dimensional observations: some austenite grains are almost completely transformed while neighbour grains are still fully austenitic. Partially formed bainite packets (one of them is delimited with black lines in Fig. 3) consist of at least two interlocking sets of parallel features (one of them is
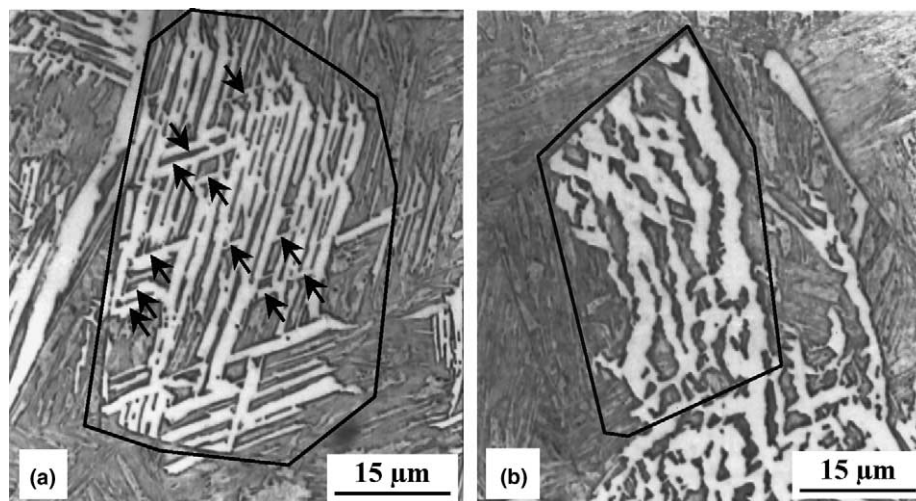
Fig. 3. Light optical micrographs of partially transformed microstructures after 1% sodium disulphite etching. (a) MI thermal cycle interrupted after 45% transformation. (b) HI thermal cycle interrupted after 30% transformation. Bainite in white, martensite in grey. Black lines delineate some of the partially formed bainite packets. Arrows in (a) indicate some parallel "bainite groups" forming a part of the bainite packet.

marked with arrows in Fig. 3(a)). These parallel features, every of them appearing as a single "grain" in the light micrographs, correspond to the "bainite groups" defined from the TEM observations. Interfaces between bainite groups and martensite (i.e., former austenite) are very straight for the medium MI cooling rate, and much more irregular for the slower HI cooling rate. The groups are probably plate-shaped, so that they sometimes appear to be "thick" in light micrographs. Consistently with TEM observations, the growth direction of groups is well defined, at least at the early stages of growth.

By careful examination of light micrographs of fully transformed microstructures (Fig. 4(a) and (b)), the bainite packets still appear as sets of groups separated by second phase particles. The HI microstructure appeared to be more "granular" than the MI microstructure, with thicker, less well defined groups. These "morphological" packets are highly intricate, in particular in the MI microstructure. Most former austenite grain boundaries are clearly visible, allowing the mean austenite grain size to be measured (Table 2). The austenite to bainite phase transformation is not complete, and numerous M–A constituents are found, in particular after the HI cycle (Table 2). Detailed size distributions of austenite grains and of second phases can be found in [9].

3.3. Bainite packet crystallography

3.3.1. Austenite to bainitic ferrite orientation relationships

In the present study, the orientation of the former austenite grains was calculated using the following method, which differs from the one used by Suh and co-workers [20,21]. The $\{001\}_\alpha$ pole figure of bainitic

ferrite within a given former austenite grain can easily be obtained using EBSD as shown in Fig. 5 for the fully transformed MI microstructure. The three Bain zones are clearly visible as indicated by numbers in Fig. 5(a). They are, in fact, centered on the $\{001\}_\gamma$ poles of the former austenite grain. The distribution of the bainite orientation within the Bain zones is not homogeneous (Fig. 5(b)), because a maximum of 24 variants of bainite can form from a given austenite grain due to the particular crystallographic orientation relationship between austenite and bainitic ferrite. The $\{001\}_\gamma$ poles, and thus the orientation of the former austenite grain, could then be readily determined using the following iterative procedure. From a first estimate of the austenite orientation, the experimental $\{001\}_\alpha$ pole figure of the bainite phase was compared with the theoretical pole figure plotted using the 24 KS and the 12 NW variants calculated from the orientation of austenite. The calculation was repeated until both experimental and calculated Bain zones matched exactly. The accuracy of the method is estimated to be around 0.5° for each of the three Euler angles. With this method, there is no need of measuring the austenite phase, and thus of retaining it. Therefore, the proposed method can be used to investigate the austenite to ferrite phase orientation relationship for any steel composition. A reconstructed pole figure is shown in Fig. 5(c). The experimental orientation relationship is well within the Bain zone, but is not necessarily exactly either the KS or NW relationship. This had already been quoted by others for upper bainite using TEM thin foil analysis [18,22–25] and for Widmanstätten kamacite (a body-centred cubic phase in iron–nickel meteorites) using X-ray synchrotron diffraction analysis [26].
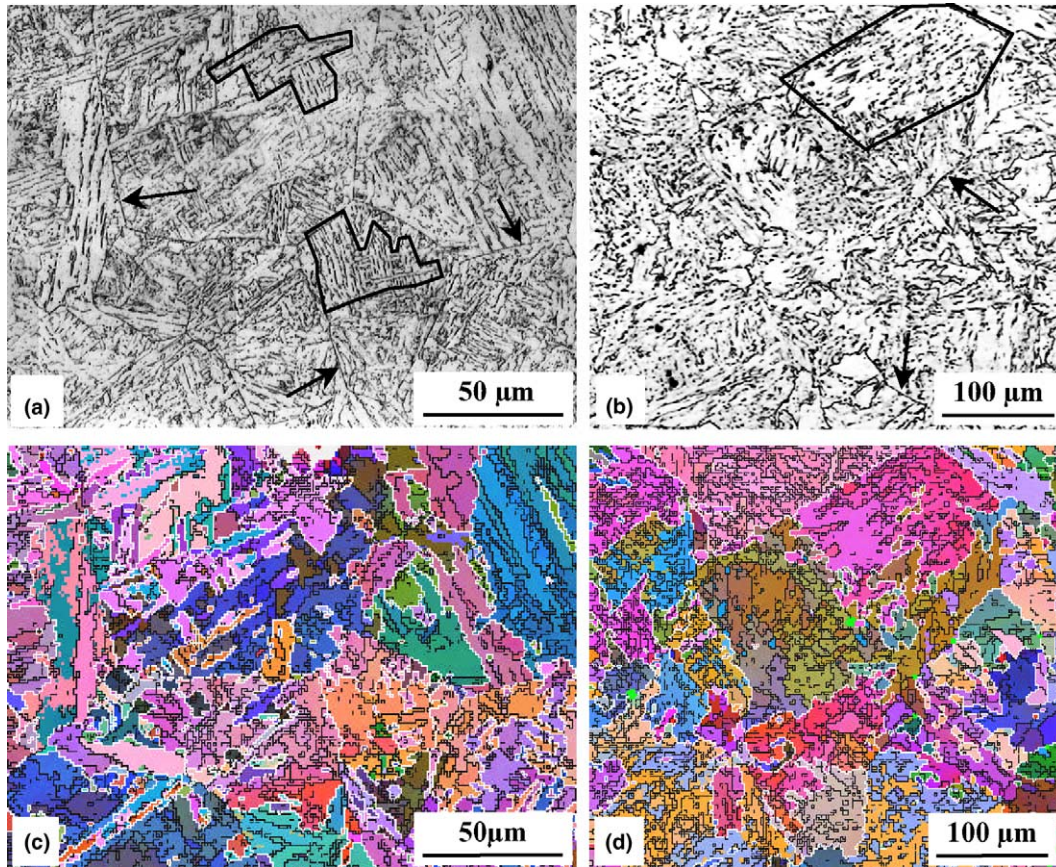
Fig. 4. Light optical micrographs obtained after (a) MI and (b) HI thermal cycles (nital etching). Corresponding EBSD maps are shown in (c) and (d), respectively, with a colour key according to the local orientation (one colour for each of the three Euler angles). Thin white and black lines indicate misorientation angles greater and lower than 20°, respectively. Morphological packets and former austenite grain boundaries are indicated with thick black lines and arrows, respectively.
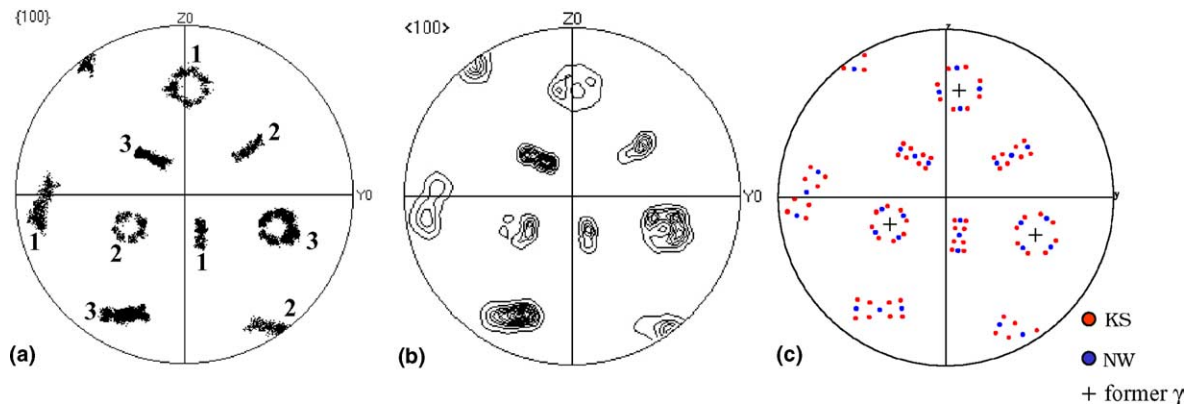

Fig. 5. $\{0\,0\,1\}_\alpha$ Pole figures from a former austenite grain in the MI microstructure. (a) Discrete and (b) density pole figure plots. (c) Orientations of the KS and NW variants calculated from the same former austenite grain. Numbers refer to the three Bain zones of the austenite phase.

3.3.2. Orientation relationships between bainite packets

The crystallographic relationships between neighbouring variants, which control cleavage microcrack propagation, were also investigated. Fig. 6(a) shows typical histograms of misorientation angle between neighbouring bainite crystals within a single former austenite grain. Obviously, only certain misorientation angles are found. These histograms were compared with theoretical histograms calculated using KS or NW orientation relationships and assuming that all pairs of neighbouring variants had the same probability to be found [7] (Fig. 6(b)). Comparison of Fig. 6(a) with 6(b)
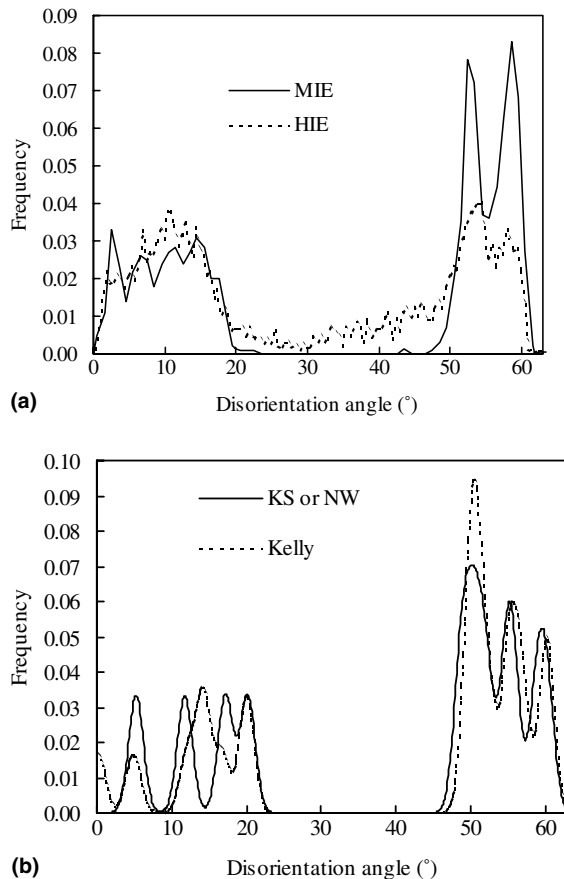
(a)

(b)

Fig. 6. Misorientation angle histogram between neighbouring bainite crystals within a single former austenite grain. (a) Experimental values. (b) Histogram computed assuming either (KS or NW) orientation relationships or 'Kelly' relationships (see Section 4.2) with austenite and no neighbourhood selection between bainite variants.

shows that low-angle boundaries are far more frequently observed than predicted by calculations. Moreover, the predicted peak around a misorientation angle of 20°, corresponding to variants in opposite locations in a given "Bain zone", was never observed experimentally. Thus, a "neighbourhood" or "local variant" selection seems to exist between bainite groups, and in particular there are "forbidden" pairs of neighbouring groups. This local variant selection has already been observed (although not always quoted) using EBSD or TEM with acicular ferrite [7], bainite [7,11,18,27] and martensite [7,12] microstructures.

3.4. Investigation of the bainite habit plane

Accurate determination of the habit plane of bainite laths is not possible, in particular in the HI microstructure, since interfaces between laths are not straight and thus not planar (Fig. 1). Here, the "habit" plane was defined as the straight, well-defined interfaces of bainite groups, which were readily observed in the partially transformed MI microstructures (Fig. 3(a)). A single-
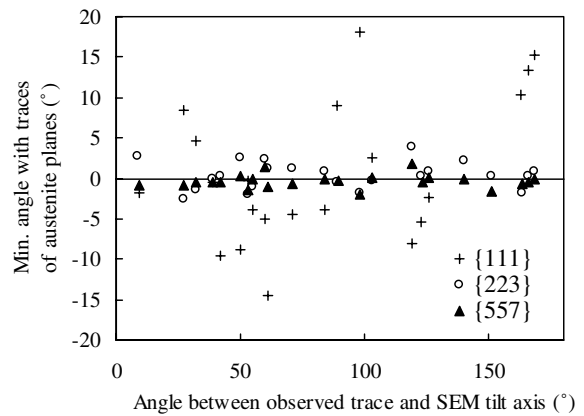

Fig. 7. Angle between the observed trace of the bainite habit plane and the closest trace of $\{111\}_\gamma$, $\{223\}_\gamma$ and $\{557\}_\gamma$ in the MI microstructure.

section trace analysis method was adopted to calculate "highly probable" indices for the habit plane. First, the crystallographic orientation of the former austenite grain was calculated from EBSD maps as explained before. Then, for each particular bainite group, the morphological and crystallographic orientations were measured and the crystallographic indices of the straight interface on the sample surface were then compared to the calculated traces of several $\{hkl\}_\gamma$ plane families. Following data on low-carbon lath martensite, and as the straight interfaces were parallel to the directions of the martensite laths in the partially transformed microstructures, three plane families were chosen, namely, $\{111\}_\gamma$, $\{223\}_\gamma$, and $\{557\}_\gamma$, as expressed in the $\langle 001 \rangle_\gamma$ frame of the austenite phase. The results are given in Fig. 7. Obviously, a significant number of traces are far from any trace of $\{111\}_\gamma$ planes. In addition, more than four directions for the interface traces were observed within a single austenite grain, and the multiplicity of the $\{111\}_\gamma$ planes in face-centred cubic austenite is only four. Thus, the $\{111\}_\gamma$ family can be discarded. The habit plane of the low-carbon bainite investigated in this study thus differs from the $\{111\}_\gamma$ planes found in steels containing 0.2–0.78 wt% carbon [28–30]. Both $\{223\}_\gamma$ and $\{557\}_\gamma$ families satisfactorily match the experimentally observed traces. As matching appears to be slightly better for the $\{557\}_\gamma$ family, it was chosen as a "highly probable" habit plane family for the investigated bainite microstructure, consistently with results already obtained with low-carbon lath martensite [12,31–33] and bainite [34].

4. Discussion and modelling

4.1. Relationships between bainite packet properties and resistance to cleavage fracture

4.1.1. Bainite packet formation
To further investigate the formation of bainite packets, a number of partially formed bainite packets
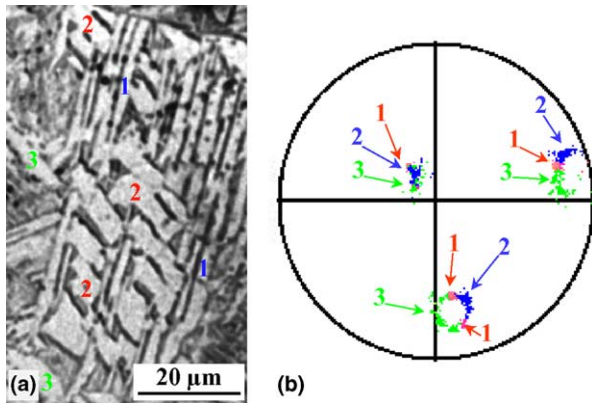
Fig. 8. EBSD investigation of a partially transformed bainite packet. MI cycle interrupted after 45% transformation. (a) Light micrograph (nital etching). (b) $\{0\,0\,1\}_\alpha$ pole figure showing that non-parallel sets labelled 1, 2 and 3 all belong to the same Bain zone of the former austenite grain.

were investigated using EBSD. As illustrated in Fig. 8, the non-parallel sets of groups always belong to the same Bain zone of the former austenite grain. As a consequence, after thickening of the sets of groups into packets, many low angle boundaries are found in the misorientation angle histograms (Fig. 6(a)). These are not easily visible after metallographic etching, so that the fully transformed microstructures appear to be "granular" and irregularly shaped. Due to the incomplete transformation phenomenon and to the intricate morphology of the groups, equiaxed, carbon-rich M–A particles are found between groups, within the packets. This complex structure and shape of bainite packets had already been observed in a detailed three-dimensional study [35]. These features could also be recognised in previous studies of "granular" or even "rectangular" [36] bainite microstructures, e.g., Fig. 8 in [37], Figs. 4, 8, 14(a) and (b) in [38], Fig. 11(b) in [39], Fig. 3 in [28] (obtained with in situ observations), and also possibly Fig. 16(a) in [40] and Fig. 1(b) in [24].

The formation of straight groups, followed by slower thickening of groups into packets could possibly be explained by considering the mechanism proposed by Ohmori et al. [28], i.e., a "martensitic-like" transformation followed by diffusion-assisted thickening. Nevertheless, this model does not consider the spatial and crystallographic configuration of bainite groups, which, in the microstructures investigated here, greatly differs from the parallel-shaped, twin-related "covariant packets" found in martensite [7,12]. In addition, other factors, including the strength of the mother austenite phase, could also influence the morphology of the bainite groups.

4.1.2. Consequences on the resistance to brittle cleavage fracture

In the fully transformed microstructures, high-angle boundaries observed in the EBSD maps (white lines in Fig. 4) delimit the "crystallographic packets" [7,8], which are the "effective packets" regarding cleavage crack propagation [8,11]. These packets are very intricate and non-convex, in particular in the MI microstructure. Due to the transformation mechanism evidenced here, and as shown in Fig. 9, crystallographic packets ('a + b' and 'c') do not necessarily correspond to morphological packets ('a' and 'b + c'). Actually, crystallographic packets frequently consist of several morphological packets. This could explain why in upper bainite cleavage microcracks often propagate without significant deviation over several morphological packets [5]. As a result, both HI and MI microstructures are more sensitive to brittle cleavage fracture than the base metal, with impact toughness transition temperatures (at 70 J) of −89, −31 and +15 °C for the base metal, MI (intricate) and HI (coarser) microstructures, respectively [9]. This is due, at least in part, to the coarse bainite matrix [41]. The mechanism of variant selection, leading to numerous low angle boundaries and thus to coarse crystallographic packets, is still unclear. In this study,
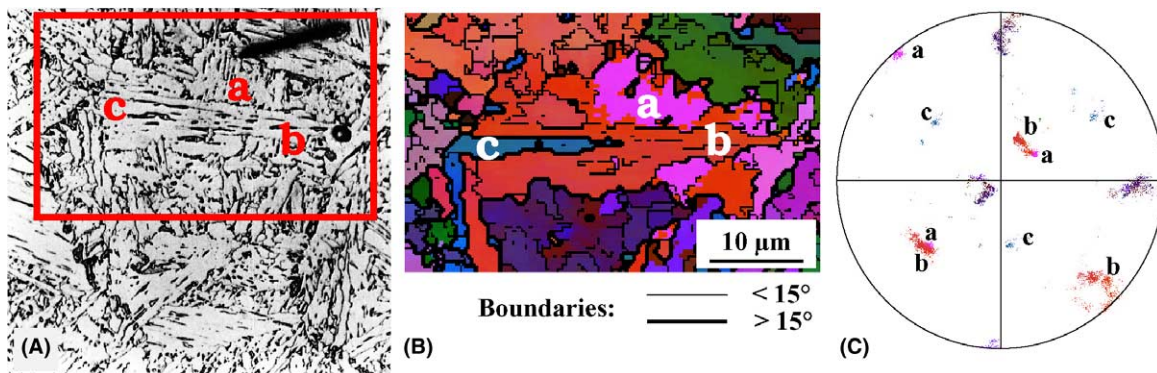

Fig. 9. High-magnification light micrograph (A) and corresponding EBSD map (B) showing that morphological packets ("a" and "b + c") do not match crystallographic packets delimited by high-angle boundaries ("a + b" and "c"). (C) Corresponding $\{0\,0\,1\}_\alpha$ pole figure showing high misorientation between crystallographic packets.

self-accommodation effects were investigated to help with resolving this issue.

4.2. Modelling the local variant selection

To tentatively account for the formation of highly intricate, plate-shaped groups of laths sharing the same Bain zone, a micromechanical model, together with a mean field homogenisation technique, was used. In this model, the formation of the groups was supposed to be accompanied by a shape strain. There are several ways to evaluate the shape strain, including surface relief measurement. In this study, surface relief was observed but not quantitatively measured. Thus, the shape strain was estimated by using the habit plane indices and a phenomenological theory of martensite crystallography (PTMC). Modelling was performed in two steps:

Step 1: Selection and use of a PTMC theory according to experimental results and calculation of the shape strain induced by the phase transformation, which is then considered as an "eigenstrain" in Step 2.

Step 2: Use of the micromechanical model to calculate the stored energy and equivalent stress in austenite induced by formation of two highly intricate sets of groups in a given austenite grain.

4.2.1. Calculation of the shape strain and crystallographic features associated with the 24 bainite variants

The habit planes in the vicinity of the $\{111\}_\gamma$ and $\{557\}_\gamma$ plane families cannot be accounted for by the PTMC theories involving a single lattice invariant shear (LIS) system [18,42]. Here, a PTMC theory involving two LIS systems was used, namely, the model developed by Ross and Crocker [43] and applied by Kelly [44] to $\{223\}_\gamma$ and $\{557\}_\gamma$ lath martensite in steels. In this theory, the ("macroscopic") shape strain is an invariant plane strain leaving the habit plane undistorted and unrotated. It is decomposed as follows:

$$\mathbf{F} = \mathbf{R} \cdot \mathbf{B} \cdot \mathbf{S_2} \cdot \mathbf{S_1}, \tag{1}$$

where $\mathbf{F}$ is the shape strain, $\mathbf{B}$ is the Bain strain induced by the homogeneous lattice transformation from face-cen-

tered cubic into body-centered tetragonal structures, and $\mathbf{S_1}$ and $\mathbf{S_2}$ are the LIS strains. Here, they correspond to slip, as no internal twinning was revealed by TEM in the bainite laths. The Bain strain only depends on the lattice parameters of the two phases and on the lattice correspondence, i.e., on the particular variant investigated. Following Kelly [44], the low-carbon bainite phase was assumed to be cubic, and the lattice correspondence was the same as the one considered in the early theory of Bowles and Mackenzie [45], leading to the following equations:

$$_\alpha\mathbf{C}_\gamma = \begin{pmatrix} 1 & 0 & 1 \\ 1 & 0 & \bar{1} \\ 0 & 1 & 0 \end{pmatrix} \tag{2}$$

is the lattice (Bain) correspondence expressed in the $\langle 001 \rangle_\alpha$ bainite frame.

$$\mathbf{B} = \begin{pmatrix} \eta_1 & 0 & 0 \\ 0 & \eta_2 & 0 \\ 0 & 0 & \eta_1 \end{pmatrix} \tag{3}$$

is the Bain strain expressed in the $\langle 001 \rangle_\gamma$ austenite frame.

The input data are as follows. Lattice parameters are 3.59 Å for austenite and 2.86 Å for bainite [46]. The slip systems were taken from [44] to lead to a $\{557\}_\gamma$ habit plane. For the variant under consideration, the shear plane and directions are $(11\bar{5})[1\bar{1}0]_\gamma$ corresponding to $(\bar{2}31)[11\bar{1}]_\alpha$ for $\mathbf{S_1}$, and $(311)[0\bar{1}1]_\gamma$ corresponding to $(211)[1\bar{1}\bar{1}]_\alpha$ for $\mathbf{S_2}$, respectively. The shear amplitudes of $\mathbf{S_1}$ and $\mathbf{S_2}$ are g_1 and g_2. Thus, the strain tensors can be expressed as follows, in the austenite frame:

for $\mathbf{S_1}$: $\mathbf{S_1} = \mathbf{I} + \dfrac{g_1}{|\mathbf{d_1}| \cdot |\mathbf{p_1}|} \cdot \mathbf{d_1} \otimes \mathbf{p_1}$, and

for $\mathbf{S_2}$: $\mathbf{S_2} = \mathbf{I} + \dfrac{g_2}{|\mathbf{d_2}| \cdot |\mathbf{p_2}|} \cdot \mathbf{d_2} \otimes \mathbf{p_2}$, $\tag{4}$

where $\mathbf{I}$ is the second-order identity tensor and for $i = 1, 2$, $\mathbf{d}_i$ is the shear direction, $\mathbf{p}_i$ is the shear plane, and g_i is the amount of shear. Following [44], the value of g_2 was chosen such that a $\{557\}_\gamma$ habit plane was obtained whatever the value of g_1, i.e., $g_2 = 0.130$.

The calculation outputs for the reference variant are the amount g_1 of first LIS $\mathbf{S_1}$, shape strain direction $\mathbf{d}$

Table 3
Results of the PTMC calculations (following [44]), expressed in the $\langle 001 \rangle_\gamma$ frame

Amount of first lattice invariant shear, g_1	0.224
Amount of macroscopic strain, m	0.490
Indices of the shape strain direction, $\mathbf{d}$	$\begin{pmatrix} 0.3138 \\ -0.8363 \\ 0.4496 \end{pmatrix}_\gamma$
Indices of the habit plane normal, $\mathbf{h}$	$(0.5025 \quad 0.5025 \quad 0.7035)_\gamma$
Angle between close-packed planes $(111)_\gamma$ and $(101)_\alpha$	0.19°
Angle between close-packed directions $[1\bar{1}0]_\gamma$ and $[11\bar{1}]_\alpha$	2.94°
Orientation relationship (axis–angle pair) between γ and α	51.15° around $\begin{pmatrix} 0.4697 \\ -0.7862 \\ 0.4017 \end{pmatrix}_\gamma$

and amplitude m, habit plane normal **h**, and orientation relationship between parent and product phases (Table 3). The habit plane of the reference variant is $(5\,5\,7)_\gamma$. Concerning the orientation relationship, the close-packed planes are not exactly parallel, as quoted in literature, e.g., [47].

The habit plane and shape strain direction were calculated for the 24 possible variants which may form in a given austenite grain. The corresponding habit plane and $\{0\,0\,1\}_\alpha$ poles are plotted in Fig. 10 in the $\langle 0\,0\,1\rangle_\gamma$ frame of the parent austenite phase. The orientation relationships between variants were also calculated together with their number fractions, under a "no local variant selection" assumption. The results are reported in Table 4. The corresponding misorientation angle histogram is reported with the "Kelly" label in Fig. 6(b), which does not greatly differ from those obtained with KS and NW. In fact, the Kelly orientation relationship is between the KS and NW orientation relationships. In the following, only the habit plane indices and shape strain are used, but the orientation relationships between austenite and bainite were experimentally observed to cluster within a few degrees around the "Kelly" one.

4.2.2. Modelling self-accommodation between two bainite variants

To qualitatively represent the highly intricate configuration of variants, a micromechanical, self-consistent scheme was used together with the Eshelby inclusion method [48]. This model enables to calculate mean stress and strain fields within each of the three phases. However, it does not take into account interface phenomena. Four pairs of variants were chosen to represent the spatial and crystallographic features observed in upper bainite and martensite microstructures. They are listed in Table 5. Calculations were carried out using a house-made computer program for reference variant 1 formed together with any of variants 1, 2, 10, or 23. Variants 1 and 2 have close habit planes and a low misorientation angle. Variants 1 and 10 have almost

Table 4
Misorientation relationships between two bainite variants within the same austenite grain as given by the γ/α orientation relationship listed in Table 3

Misorientation angle (°)	Low-index axis family	Offset (°)	Pairs of variants
0.0	–	–	1–1
4.7	$\{0\,1\,1\}_\alpha$	4.0	1–2
11.9	$\{1\,3\,3\}_\alpha$	1.6	1–10
14.1	$\{0\,2\,3\}_\alpha$	3.6	1–3, 1–5
16.6	$\{1\,3\,3\}_\alpha$	0.9	1–7
19.9	$\{0\,1\,4\}_\alpha$	5.5	1–22
19.9	$\{0\,1\,4\}_\alpha$	3.6	1–4
49.3	$\{1\,1\,1\}_\alpha$	4.1	1–20
50.0	$\{3\,3\,4\}_\alpha$	3.8	1–18, 1–19
50.5	$\{1\,3\,3\}_\alpha$	1.6	1–16, 1–17
50.8	$\{2\,3\,3\}_\alpha$	0.1	1–21
52.3	$\{1\,3\,3\}_\alpha$	3.5	1–6, 1–8
55.0	$\{1\,3\,3\}_\alpha$	1.9	1–9, 1–11
55.4	$\{0\,1\,1\}_\alpha$	0.3	1–24
56.8	$\{1\,3\,3\}_\alpha$	2.9	1–14, 1–15
60.0	$\{0\,1\,1\}_\alpha$	0.3	1–12, 1–13
60.3	$\{3\,3\,4\}_\alpha$	2.2	1–23

"Offset" is the angle between the actual rotation axis and the closest low-index axis.

perpendicular habit planes and a low misorientation angle. Variants 1 and 23 have the same habit plane but are highly misoriented (5.6° from the twin misorientation relationship).

Use of the Eshelby inclusion method enables to take into account the geometry of the phases. The austenite phase was assumed to be isotropic. Each of the "plate-like" bainite variants (in fact, each set of parallel groups as explained before) was modelled as a flat ellipsoidal inclusion having a shape ratio of 1:20, consistently with experimental observations, and minor axis normal to its habit plane. The ellipsoid shape allows the stresses and strains to be homogeneous in the inclusion. The volume fractions of phases were 0.25 for the first variant, 0.25 for the second variant, and 0.5 for untransformed austenite, consistently with metallographic observation of many partially transformed bainite packets (e.g., Fig. 3(a)).
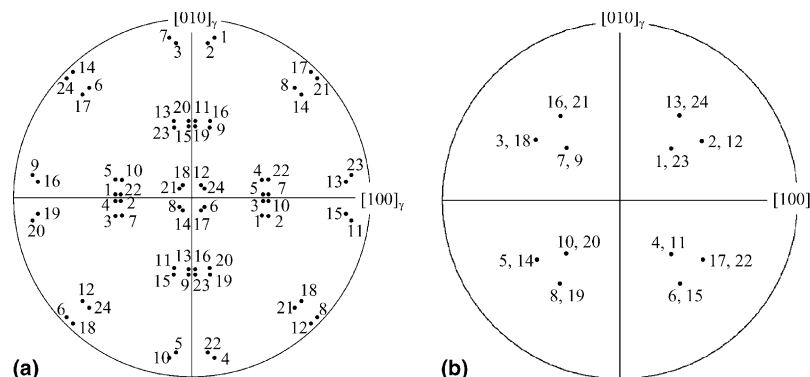

Fig. 10. (a) $\{0\,0\,1\}_\alpha$ and (b) $\{5\,5\,7\}_\gamma$ habit plane pole figures calculated using the PTMC model. Numbers refer to the 24 possible variants.

Table 5
Results given by self-consistent modelling of accommodation between bainite variants

Pair of variants	Habit plane of second variant	Angle between habit planes	Misorientation angle	Stored elastic energy	Mean Von Mises equivalent stress in bainite (MPa)	Mean Von Mises equivalent stress in austenite (MPa)
1–1	$(5\,5\,7)_\gamma$	0°		1.00	392	392
1–2	$(\bar{7}\,5\,5)_\gamma$	16.3°	4.7°	1.39	534	377
1–10	$(\bar{5}\,\bar{5}\,7)_\gamma$	89.4°	11.9°	1.72	654	321
1–23	$(5\,5\,\bar{7})_\gamma$	0°	60.3°	1.53	614	308

The value of stored energy is normalised by the value obtained for 50% of variant 1 alone.

The homogenisation method used a self-consistent scheme, although the underlying hypothesis of "perfect disorder" in the three-phase microstructure might not be fulfilled in the present case. Each of the three phases was in turn considered as an "Eshelby" inclusion embedded in an infinite matrix having the average ("homogenised") properties of the three-phase material [49]. Stress-free boundary conditions were applied to the infinite matrix. The elastic properties of the phases were assumed to be homogeneous and isotropic. Thus, coupling between phases only derives from the self-consistency assumption and from the disappearance of the mean stress tensor far from the inclusions.

Each inclusion I ($I = \gamma$ for austenite, $I = 1$ for variant 1, $I = N$ for the other variant, with $N = 1, 2, 10$, or 23) was attributed a fourth-order Eshelby tensor $\mathbf{S^I}$ (representing its geometry) and a second-order eigenstrain tensor ε_I^*. For bainite variants 1 and N, ε_I^* is the transformation-induced shape strain determined in the previous section. The bainite variants were considered to remain elastic but plastic deformation was allowed in the austenite phase. Thus, ε_γ^* is the amount of plastic strain induced in austenite by the transformation of the two other phases. It was calculated using an iterative method by assuming an elastic–plastic constitutive behaviour for the austenite phase. The accuracy of values used for the coefficients does not affect the trends given by the model but affects the quantitative values, so that the following results can only be interpreted in a qualitative manner. Here, as a first step, the values were set as follows: Young's modulus $E = 2 \times 10^5$ Pa and Poisson ratio $v = 0.3$ for all phases, and for austenite, a yield strength of 300 MPa and an isotropic linear work-hardening rate of 5000 MPa. At each iteration step, the difference between the equivalent Von Mises stress in austenite and the yield stress given by the constitutive equation for the same equivalent plastic strain was calculated. If negative, the plastic strain amplitude was slightly increased along the normal to the Von Mises yield surface of the austenite phase. Convergence of results was reached as soon as the equivalent stress in the austenite phase was equal to the stress predicted using the constitutive equation and total equivalent strain in austenite. The total number of iterations was less than 100.

The equations used in the homogenisation model are as follows. The uniform stress in inclusion I is:

$$\sigma_I = \mathbf{C} : (\mathbf{I} - \mathbf{S^I}) : (\mathbf{E}^* - \varepsilon_I^*), \quad \text{(Eshelby inclusion problem)} \tag{5}$$

where $\mathbf{C}$ is the fourth-order elasticity tensor, $\mathbf{I}$ is the fourth-order identity tensor and $\mathbf{E}^*$ is the average eigenstrain tensor, which is derived from the stress-free boundary conditions:

$$\langle \mathbf{I} - \mathbf{S^I} \rangle : \mathbf{E}^* = \langle (\mathbf{I} - \mathbf{S^I}) : \varepsilon_I^* \rangle, \tag{6}$$

where "$\langle \cdot \rangle$" denotes averaging over all three phases.

The calculations were carried out in the frame of the ellipsoid of variant 1. To solve the Eshelby problem, a small-scale deformation hypothesis had to be made, so that only the symmetric part of the shape strain matrices could be considered. Consistently with this, the shape strain amplitude was divided by ten, in order to satisfy the small-scale deformation assumption. This should not qualitatively affect the comparison between results obtained with the various pairs of variants.

4.2.3. Results given by the model

The stored energy (normalised by the value obtained with variant 1 alone i.e., $N = 1$) is given in Table 5 together with the Von Mises equivalent stress in the austenite phase. In terms of stored elastic energy, the most efficient accommodation is given by the single-variant configuration. This could explain why parallel groups of a given variant are frequently seen in micrographs (Fig. 3(a)). Nevertheless, this could also be at least partly due to the assumption of homogeneous and isotropic elastic properties of the material, while the micromechanical model handles with geometric and crystallographic features at the scale of the individual crystals. The mechanical behaviour of bainite also plays a significant role, as the major part of the elastic stored energy stems from the high stresses in the bainite inclusion. Allowing plastic deformation in bainite should significantly change the values of the energy stored in the system.

In terms of stress and plastic strain in the austenite phase, the single-variant configuration is clearly the less accommodating configuration. Variant 2, having the lowest misorientation with variant 1, does not allow

significant strain accommodation. Both variants 10 and 23 help accommodating the strain resulting from the transformation of variant 1. Variant 23 was not experimentally observed to be intimately associated with variant 1, consistently with previous literature results on upper bainite [18]. It is worth noting that the misorientation relationship between variants 1 and 23 slightly departs from the twin relationship, so that the transformation eigenstrains of variants 1 and 23 do not cancel each other. On the other hand, low-angle misorientation between groups of laths having highly misoriented habit planes, such as variant 10 with variant 1, were most frequently observed in the investigated microstructures. The model indicates that this particular spatial and crystallographic arrangement is able to partly accommodate the transformation strain by limiting plastic deformation in the austenite phase. This could in turn help growth of the bainite phase, which is known to be hindered or eventually stopped by increasing plastic strain in the mother austenite phase [50]. Thus, the model shows how self-accommodation can be at least partly achieved thanks to the experimentally observed configuration. Further work is still in progress to more accurately describe interactions between neighbouring bainite variants during the phase transformation.

5. Summary and conclusions

The present study was devoted to the formation of upper bainite in a high strength, low alloy steel under simulated welding conditions. No particular hypothesis was made concerning the actual transformation mechanism at the interface. Multi-scale crystallographic and metallographic investigations together with simple analytical micromechanical modelling led to the following results:

1. The EBSD technique is able to give detailed crystallographic features of the phase transformation, including orientation relationships with the mother austenite phase even if no retained austenite is analysed. The proposed method can thus be used for any steel chemical composition. In this study, the orientation relationship between parent and product phases is well within the Bain zone, and close to the KS or NW relationships.
2. Upper bainite packets of the fully transformed microstructures consist of highly intricate, non-parallel sets of plate-shaped groups of laths. These groups have a low angle misorientation relationship but highly misoriented habit planes.
3. The bainite phase transformation appears to occur in two stages. In the first stage, discrete, non-parallel, highly intricate, straight groups of laths form. The second stage is thickening of these groups, leading to coarse crystallographic packets containing both elongated and equiaxed M–A constituents.
4. Simple analytical micromechanical modelling of accommodation mechanism was carried out by solving an Eshelby inclusion problem using a self-consistent scheme. Results indicate that the intricate configuration described above could be able to limit the plastic strain in austenite, and thus to enhance growth of the bainite phase.

References

[1] Akselsen OM, Solberg JK, Grong Ø. Scand J Metall 1988;17: 194.
[2] Kim BC, Lee S, Kim NJ, Lee DY. Metall Trans A 1991;22:139.
[3] Matsuda F, Ikeuchi K, Okada H, Hrivnak I, Park HS. Trans JWRI 1994;23:231.
[4] Naylor JP, Krahe PR. Metall Trans 1974;5:1699.
[5] Pickering FB. The structure and properties of bainite in steels. In: Proceedings of the Transformation and Hardenability in Steels. Ann Harbor, MI: Climax Molybdenum; 1967. p. 109.
[6] Brozzo P, Buzzichelli G, Mascanzoni A, Mirabile M. Met Sci 1977;11:123.
[7] Gourgues AF, Flower HM, Lindley TC. Mater Sci Technol 2000;16:26.
[8] Bouyne E, Flower HM, Lindley TC, Pineau A. Scripta Mater 1998;39:295.
[9] Lambert-Perlade A, Gourgues AF, Besson J, Sturel T, Pineau A. Metall Mater Trans A 2004 [in press].
[10] Kluken AO, Grong Ø, Hjelen J. Metall Trans A 1991;22:657.
[11] Kim M-C, Oh YJ, Hong JH. Scripta Mater 2000;43:205.
[12] Morito S, Tanaka H, Konishi R, Furuhara T, Maki T. Acta Mater 2003;51:1789.
[13] Mehl RF. Hardenability of alloy steels. Cleveland, OH: ASM; 1939. p. 1.
[14] Ohmori Y, Ohtsubo H, Jung YC, Okaguchi S, Ohtani H. Metall Mater Trans A 1994;25:1981.
[15] Kurdjumov G, Sachs G. Z Phys 1930;64:325.
[16] Nishiyama Z. Sci Rep Res Inst, Tôhoku University 1934;23:637.
[17] Wassermann G. Arch Eisenhüttenwes 1933;6:347.
[18] Sandvik BPJ. Metall Trans A 1982;13A:777.
[19] Kalwa G, Schnabel E, Schwaab P. Steel Res 1986;5:207.
[20] Suh DW, Kang JH, Oh KH, Lee HC. Scripta Mater 2002;46:375.
[21] Cho JY, Suh DW, Kang JH, Lee HC. ISIJ Int 2002;42:1321.
[22] Luo CP, Weatherly GC, Liu Z-Y. Metall Trans A 1992;23:1403.
[23] Ohmori Y. The crystallography and the mechanism of upper bainite formation. In: Inoue K, Mukherjee K, Otsuka K, Chen H, editors. Displacive phase transformations and their applications in materials engineering, the minerals. Metals Park, OH: Metals and Material Society; 1998. p. 85.
[24] Zhang M-X, Kelly PM. Scripta Mater 2002;47:749.
[25] Moritani T, Miyajima N, Furuhara T, Maki T. Scripta Mater 2002;47:193.
[26] Bunge HJ, Weiss W, Klein H, Wcislak L, Garbe U, Schneider JR. J Appl Crystallogr 2003;36:137.

[27] Matsuoka S, Sakata K, Furukimi O, Obara T. Orientational morphology of low carbon steel rolled in nonrecrystallized austenite region. In: Koiwa M, Otsuka K, Miyazaki T, editors. International Conference of the Solid-Solid Phase Transformations '99. Sendai, Japan: The Japan Institute of Metals; 1999. p. 1537.

[28] Ohmori Y, Jung Y-C, Nakai K, Shioiri H. Acta Mater 2001;49:3149.

[29] Smith GV, Mehl RF. Trans AIME 1942;150:211.

[30] Sarikaya M, Tokushige H, Thomas G. Lath Martensite and Bainite in Low Alloy Steels. In: Proceedings of the International Conference of Martensitic Transformations. Sendai, Japan: The Japan Institute of Metals; 1986. p. 613.

[31] Sandvik BPJ, Wayman CM. Metall Trans 1983;14:809.

[32] Marder AR, Krauss G. Trans ASM 1990;62:957.

[33] Kelly PM, Jostsons A, Blake RG. Acta Metall Mater 1990;38:1075.

[34] Ohmori Y, Maki T. Mater Trans JIM 1991;32:631.

[35] Hackenberg RE, Nordstrom DP, Shiflet GJ. Scripta Mater 2002;47:357.

[36] Tian D, Pentti Karjalainen L, Qian B, Chen X. Scand J Metall 1996;25:87.

[37] Liu SK, Zhang GY. Metall Trans A 1990;21:1509.

[38] Reynolds Jr WT, Liu SK, Li FZ, Hartfield S, Aaronson HI. Metall Trans A 1990;21:1479.

[39] Liu SK, Yang L, Zhu DG, Zhang J. Metall Mater Trans A 1994;25:1991.

[40] Bramfitt BL, Speer JG. Metall Trans A 1990;21:817.

[41] Lambert-Perlade A, Gourgues AF, Sturel T, Pineau A. Fracture Toughness of Simulated HAZ in HSLA Steel Welds. In: Miannay D, Costa P, François D, Pineau A, editors. Proceedings of the Euromat'2000 Advances in Mechanical Behaviour, Plasticity and Damage. Amsterdam: Elsevier; 2000. p. 97.

[42] Bowles JS, Kennon NF. J Aus Inst Met 1960;5:106.

[43] Ross NDH, Crocker AG. Acta Metall 1970;18:405.

[44] Kelly PM. Mater Trans JIM 1992;33:235.

[45] Bowles JS, Mackenzie JK. Acta Metall 1954;2:224.

[46] Lambert-Perlade A. Ph.D dissertation, Ecole des Mines de Paris, Paris, France, 2001, p. 117.

[47] Christian JW. Metall Trans A 1990;21:799.

[48] Eshelby JD. Proc Roy Soc A 1957;241:376.

[49] François D, Pineau A, Zaoui A. In: Mechanical behaviour of materials, vol. I. Dordrecht, The Netherlands: Kluwer Academic Publishers; 1998. p. 100.

[50] Bhadeshia HKDH. Bainite in steels. London: The Institute of Materials; 1992. p. 9.